

# Gas storage, transport and pressure changes in an evolving permeable volcanic edifice

A.S.D. Collinson\*, J.W. Neuberg

School of Earth and Environment, The University of Leeds, Leeds LS2 9JT, UK

## ARTICLE INFO

### Article history:

Received 16 April 2012

Accepted 22 June 2012

Available online 3 July 2012

### Keywords:

Permeability

Darcy's law

Volcanic degassing

Gas pressure

## ABSTRACT

The total volume of gas in a magma, dissolved and subsequently exsolved, greatly influences the degree of explosiveness of a volcanic system. There is a marked contrast between the behaviour of a volcano in an “open” system compared to one which is “closed”. It is therefore essential to understand the entire degassing process: gas transport, storage and loss. A particular focus of this study is the effect different permeabilities and pressure gradients within a volcanic edifice have on the degree and pattern of the gas velocity. Gas loss is modelled numerically in two dimensions using a finite element approach, which allows the specification of boundary conditions with respect to pressure and different permeability domains within the volcanic edifice. By combining the time-dependent continuity equation and Darcy's law, a partial differential equation is derived and solved for the pressure. The associated pressure gradient is then used within Darcy's law to determine the corresponding gas velocity distribution. This method is used not only for stationary systems in equilibrium, but also as a time-dependent progression. It permits the modelling of different situations to study how various volcanic characteristics affect the gas loss. The model is used to investigate the change in pressure and gas in response to time-dependent scenarios. These are a dome collapse or sudden increase in permeability by magma rupture at the conduit margin, the formation of cracks within the lava dome and sealing by crystallisation.

Our results show that a combination of high and low permeability regions is required for effective gas storage. High permeability allows the gas to enter the system, but impermeable areas act to confine the gas, thereby increasing its pressure and consequently, increasing the amount of gas which may be dissolved in the melt. Furthermore, our results show that permeability is an essential factor influencing the response time to system changes, which could be linked in future to deformation and other geophysical observations. Our model is highly versatile and sheds new light on the understanding of gas storage and transport in a permeable volcanic edifice.

© 2012 Elsevier B.V. All rights reserved.

## 1. Introduction

The degassing behaviour of a volcano is intimately related to the permeability, and how the permeability evolves through time. As stated by Jaupart and Allègre (1991), the ability for a volcanic system to degas is directly tied to the availability of degassing pathways, and the existence of a driving pressure. Such conditions have been investigated by a number of studies, many of which have derived models incorporating Darcy's law, such as the permeable foam model of Taylor et al. (1983) and Eichelberger et al. (1986), expanded further by the addition of horizontal degassing through the conduit walls proposed by Jaupart and Allègre (1991). Edmonds et al. (2003) used a form of Darcy's law to model the SO<sub>2</sub> flux on Soufrière Hills volcano with respect to permeability. Additionally, other potential pathways include horizontal fractures (Jaupart, 1998), complementing the drilled field evidence found at Obsidian Dome (Heiken et al., 1988) and the near-horizontal tuffsite veins at Mule Creek (Stasiuk et al., 1996). There are several examples of measured permeabilities for volcanic eruption products (e.g. Eichelberger

et al., 1986; Klug and Cashman, 1996; Melnik and Sparks, 2002), but unsurprisingly, none for the real-time evolution of the active magma conduit. Eichelberger et al. (1986) provide six permeability values for Inyo Rhyolite with a range from 10<sup>−12</sup> to 10<sup>−8</sup> m<sup>2</sup>. Klug and Cashman (1996) measured the permeability of Plinian pumice products providing data ranging from 10<sup>−13</sup> to 7 × 10<sup>−12</sup> m<sup>2</sup> (for samples with 70–90% vesicularity) and 10<sup>−14</sup> to 2 × 10<sup>−13</sup> m<sup>2</sup> (for those with 30–50% vesicularity). Bernard et al. (2007) measured permeabilities and porosities for 48 samples (mainly pyroclastic eruption products) from Montagne Pelée and obtained ranges of 3 to 62% and 10<sup>−16</sup> to 35 × 10<sup>−12</sup> m<sup>2</sup> for porosity and permeability respectively. Additionally, they measured the anisotropy of samples, and found a large disparity of 28 to 162% between directions in samples. Similarly, Tait et al. (1998) discovered a 50% variance in anisotropy directions in pumices from the Minoan plinian eruption of Santorini. The range of permeability values they obtained lies in the region of 8 × 10<sup>−13</sup> to 10<sup>−11</sup> m<sup>2</sup> for 75–80% vesicularity. Mueller et al. (2005) made permeability measurements of a variety of samples from a number of different volcanoes, including Merapi (Indonesia), Pinatubo (Philippines) and Mt. Unzen (Japan) and derived porosity values ranging between 4 and 84% and permeability values of 2.5 × 10<sup>−15</sup> to 7.6 × 10<sup>−12</sup> m<sup>2</sup>. Melnik and Sparks (2002) measured samples of the Soufrière Hills andesite and

\* Corresponding author. Tel.: +44 113 3436769.

E-mail addresses: [a.collinson@see.leeds.ac.uk](mailto:a.collinson@see.leeds.ac.uk) (A.S.D. Collinson), [j.neuberg@leeds.ac.uk](mailto:j.neuberg@leeds.ac.uk) (J.W. Neuberg).

derived permeability values between approximately  $6 \times 10^{-16}$  and  $5 \times 10^{-12} \text{ m}^2$ . Bouvet de Maisonneuve et al. (2009) measured permeability and porosity for silicic pumices of the Kos Plateau Tuff (East Aegean Arc) and derived values ranging  $10^{-14}$  to  $10^{-11} \text{ m}^2$ . Wright et al. (2006) measured the permeability of anisotropic tube pumice clasts from four different rhyolitic pyroclastic flow and fall deposits, and obtained values ranging from  $2 \times 10^{-15}$  to  $10^{-10} \text{ m}^2$ . In Wright et al. (2009) these results were compared with three other deposit types, namely dacitic vulcanian breadcrust bombs, Glass Mountain pumice fall deposits and obsidian flow clasts, and a variety of samples of andesitic origin. They demonstrate variations in permeability and porosity trends that reflect the varying composition, setting and eruption styles.

Permeability and porosity studies have also been performed on synthetic eruption products (e.g. Takeuchi et al., 2005; Laumonier et al., 2011), whilst others have investigated the relationship between magma permeability and the resulting volcanic activity (e.g. Spieler et al., 2004; Burgisser and Gardner, 2005; Mueller et al., 2008).

Today, via a combination of experimental (e.g. Mader et al., 1994, 1997) and numerical (e.g. Melnik and Sparks, 1999, 2002; Gonnermann and Manga, 2005; Papale et al., 2006; Burgisser et al., 2010; de' Michieli Vitturi et al., 2010; Yoshimura and Nakamura, 2011) exsolution studies, we have a relatively good understanding of how a multi-component volatile phase exsolves from magma. However, at crystal-rich intermediate arc volcanoes, it has become evident that switches in eruption style, and cyclic eruptive activity, are strongly dependent on whether permeable degassing pathways exist for the exsolved vapour to escape from the system (e.g. Edmonds et al., 2003; Edmonds and Herd, 2007). The impact of variable permeability can be profound: a growing lava dome may progressively “seal” due to gas loss during ascent, microlite growth (e.g. Melnik and Sparks, 1999; Cashman and Blundy, 2000; Couch et al., 2003; Clarke et al., 2007; de' Michieli Vitturi et al., 2010; Melnik et al., 2011) and vapour phase crystallisation of cristobalite in pore spaces (e.g. Boudon et al., 1998; Baxter et al., 1999), causing pressurisation which may induce lava dome collapse. In this scenario, the associated decompression leads to a dramatic increase in gas flux and explosive activity. Tantalising hints of these sealing and pressurisation processes are documented in records of gas flux at many volcanoes (e.g. Fischer et al., 1996; Williams-Jones et al., 2001; Edmonds et al., 2003). For instance, at Soufrière Hills volcano: (1) gas fluxes progressively decline as the lava dome gets larger and older (Edmonds et al., 2003); (2) large gas clouds are observed after lava dome collapses suggesting significant gas storage in the shallow conduit and lava dome prior to collapse (MVO, 2006). In contrast, fractures can develop within the dome due to magma extrusion or the weight of the dome. In addition, seismically-induced fractures may occur within the conduit (Neuberg et al., 2006).

In this study, we consider the situation of a static magma column where the gas is provided by a deeper source, and not by the magma flow itself. However, in the case of pressure changes, additional sources due to exsolution of gas are considered. In contrast to Collombet (2009), where an attempt was made to reduce the gas content in a numerical conduit flow model by arbitrary iteration steps, we separate the degassing problem from the magma flow in order to model its time dependence. This case corresponds to a volcano that has stopped extrusion and continues to degas. The aim of this study is to investigate the interaction between permeability and pressure to estimate the pressure gradients that control gas storage and escape routes at shallow levels within the volcanic edifice. We address the question of whether a dome collapse can be triggered by pressurisation due to an impermeable overburden, as proposed by Stix et al. (1993) for Galeras, and the role of pressurisation during the formation of fracture zones potentially leading to accelerated magma ascent (Edmonds and Herd, 2007).

## 2. Method and computational setup

The equations describing gas loss from a static magma are solved numerically in two-dimensions for either axisymmetric (to model a

cylindrical conduit) or Cartesian (to model a dyke) coordinate systems. Except for the principal block model, we show only the results for a dyke. The system was solved using a finite element approach in COMSOL Multiphysics V4.2 where the spatial and temporal resolutions were tested. Using the variables from Table 1, the equations for Darcy's law (Eq. (1)) and the continuity equation (Eq. (2)) are combined to derive a partial differential equation (Eq. (3)) which is solved for the pressure. The associated pressure gradient is used within Darcy's law to determine the gas flux. The gas was modelled as  $\text{H}_2\text{O}$  with the density calculated using the mean molecular mass within the ideal gas law (Eq. (4)) and the viscosity given a constant value of  $1.5 \times 10^{-5} \text{ Pas}$ . Computations are carried out as both static geometries in equilibrium and time-dependent sequences.

$$u = -\frac{k}{\mu}(\nabla P + \rho g \nabla z) \quad (1)$$

$$\frac{\partial}{\partial t}(\rho \epsilon) + \nabla \cdot (\rho u) = Q_m \quad (2)$$

$$\frac{\partial}{\partial t}(\rho \epsilon) + \nabla \cdot \rho \left[ -\frac{k}{\mu}(\nabla P + \rho g \nabla z) \right] = Q_m \quad (3)$$

$$\rho = \frac{M}{RT} P \quad (4)$$

$$P_{\text{lith}} = P_{\text{atm}} + \rho_r g z \quad (5)$$

$$P_{\text{op}} = P - P_{\text{lith}} \quad (6)$$

$$\frac{\partial}{\partial t} \nabla \cdot (\nabla n_{\text{ex}} \rho_r) = Q_m \quad (7)$$

$$n_{\text{ex}} = n_{\text{tot}} - K \sqrt{P} \quad (8)$$

A general model geometry is depicted in Fig. 1. Models are created to represent a magma-filled conduit embedded in a volcanic edifice, and a lava dome with cracks and layers of different permeabilities. The exterior boundaries of the dome are set to atmospheric pressure ( $P_{\text{atm}}$ ). The base of the conduit and all other exterior boundaries are set to lithostatic pressure ( $P_{\text{lith}}$ ) (Eq. (5)). For the time-dependent models, the initial conditions are set either to lithostatic pressure or to the solution from a previously solved static model. The gas overpressure is calculated according to Eq. (6). In the case of the dome collapse, we

**Table 1**  
Parameters used in the modelling.

Symbol	Units	Description
$u$	$\text{ms}^{-1}$	Gas volume flux
$k$	$\text{m}^2$	Host permeability
$\mu$	$1.5 \times 10^{-5} \text{ Pas}$	Gas viscosity
$P$	Pa	Gas pressure
$P_{\text{lith}}$	Pa	Lithostatic pressure
$P_{\text{op}}$	Pa	Gas overpressure
$P_{\text{atm}}$	$0.1 \times 10^6 \text{ Pa}$	Atmospheric pressure
$\rho$	$\text{kg m}^{-3}$	Gas density
$\rho_r$	$2500 \text{ kg m}^{-3}$	Rock density
$g$	$9.81 \text{ ms}^{-2}$	Acceleration due to gravity
$z$	m	Unit vector in the vertical
$t$	s	Time
$\epsilon$		Host porosity
$Q_m$	$\text{kg m}^{-3} \text{ s}$	Mass source term
$M$	$0.017 \text{ kg mol}^{-1}$	Molecular mass
$R$	$8.314 \text{ m}^3 \text{ Pa K}^{-1} \text{ mol}^{-1}$	Ideal gas constant
$T$	1123 K	Temperature
$z$	m	Vertical vector
$n_{\text{ex}}$	wt.%	Exsolved gas
$n_{\text{tot}}$	wt.%	Total gas
$K$	$4.11 \times 10^{-6} \text{ Pa}^{-\frac{1}{2}}$	Solubility constant for silicic magma

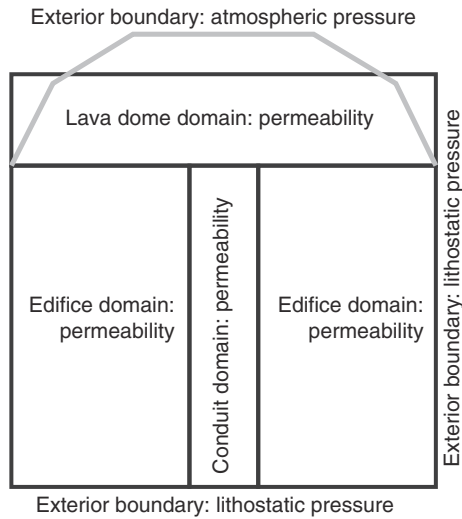


Fig. 1. General model configuration.

introduce a source term to account for additional sources of gas due to exsolution (Eqs. (7) and (8)).

The pressures and permeabilities are either constant, or altered continuously or intermittently through time in a more complex time-dependent model. The subsequent exsolution of gas due to pressure changes is not explicitly modelled, but the effects are qualitatively discussed.

### 3. Models and results

In the following, our numerical simulations were used to model the shallow processes of degassing taking place under different conditions. Investigated structural features include cracks in the dome and areas of differing permeability. The results are plotted on the model geometry surface (Fig. 1) as pressure, and logarithmic arrows show the direction of the gas velocity, which are colour-coded to indicate the magnitude, increasing from black to white. The permeability and porosity values used within each model are listed in Table 2. Where time dependence is considered, we find that the time to reach equilibrium is proportional to the inverse of the permeability. An example of this time scale is given for each model.

#### 3.1. Principal block model

Simple “block-style” models represent a simplified concept of a volcanic system at shallow levels. They encompass a central magma-filled block (“conduit”), surrounded on both sides by the “wall rocks” of the volcanic edifice, and topped by an overburden (“lava dome”). Whilst permeability in the volcanic edifice ranges from  $10^{-12}$  to  $10^{-16}$  m<sup>2</sup> (e.g. Klug and Cashman, 1996; Melnik and Sparks, 2002; Mueller et al., 2005), we chose to simulate a high permeability within the conduit with  $10^{-10}$  m<sup>2</sup> which provides the maximum pressurisation.

We assume the gas originates from the magma; therefore, we chose the permeability within the conduit to be higher due to the connected gas pathways. In contrast, the country rock consists of compacted lithologies resulting in a lower permeability.

The gas flow and pressure distribution are strongly dependent upon the relative permeabilities within the system. An open system occurs whereby the permeability within all domains is sufficient to enable unimpeded gas flow throughout. In contrast a closed system may be generated when one or more of the domains is either completely or partially impermeable. Fig. 2a shows an open system, where gas is free to escape. The highest permeability occurs within the conduit and although the permeability within the walls and

Table 2  
Permeability and porosity settings for each model.

Model	Figure	Region	Porosity	Permeability (m <sup>2</sup> )	
				<i>t</i> <sub>1</sub>	<i>t</i> <sub>2</sub>
Principal block	2	Conduit	0.3	$10^{-10}$	–
		Edifice	0.3	$10^{-12}$	–
		Overburden	0.3	$10^{-12}$	–
	2b	Edifice	0.3	$10^{-12}$	–
		Overburden	0.3	$10^{-16}$	–
	2c	Edifice	0.3	$10^{-16}$	–
Sealing gas escape routes	9	Overburden	0.3	$10^{-16}$	–
		Conduit	0.5	$10^{-10}$	–
		Edifice	0.3	$10^{-12}$	–
		Sealed edifice	0.1	$10^{-12}$	$10^{-16}$
		Spine	0.1	$10^{-12}$	$10^{-16}$
Cracked dome model	11	Conduit	0.5	$10^{-10}$	–
		Edifice	0.3	$10^{-14}$	–
		Dome	0.3	$10^{-14}$	–
		Cracks	0.3	$10^{-14}$	$10^{-8}$
		Fracture zones	0.1	$10^{-16}$	$10^{-6}$
Gas escape in fracture zones	14, 15, 17	Conduit	0.5	$10^{-10}$	–
		Edifice	0.3	$10^{-12}$	–
		Fracture zones	0.1	$10^{-16}$	$10^{-6}$
Dome collapse	18	Conduit	0.3	$10^{-10}$	–
		Edifice	0.3	$10^{-16}$	–
		Overburden	0.3	$10^{-16}$	$10^{-6}$
		Overburden	0.3	$10^{-16}$	$10^{-6}$

overburden is lower than that of the conduit, it is still sufficiently high to permit gas transfer. Fig. 2b is a partially closed system due to a sealed overburden, whereas in Fig. 2c the conduit is completely surrounded by less permeable layers. The surface plots of all three models are on the same scale, so it is obvious that there is less pressurisation within the open system. The span of permeability conditions expresses well the ability for the impermeable layer to trap the gas, invoking a build-up of pressure. In each model, the highest pressure occurs at the base of the conduit due to the lithostatic pressure. In contrast to the open system, sealing the overburden results in higher pressure being maintained to shallower levels within the conduit, in addition to pressurisation within the “dome”. Fig. 2c maintains pressurisation throughout the extent of the conduit, and into the walls and overburden. In all the “sealed” regions, gas flow appears negligible (with a dominance of black arrows over grey).

The pressure pattern within the closed system (Fig. 2c) is very similar to that in the open system (Fig. 2a) because the relative permeability within the walls and dome is the same. However, in the closed system, the permeability of these two regions is lower than the equivalent in the open system. Modifying either wall or dome separately results in a more complex pattern of pressurisation.

Fig. 3 shows the overpressure imposed by the gas (by subtracting lithostatic pressure). They show that the greatest overpressure is concentrated at the top of the conduit. In Fig. 3a the overpressure is lower due to the higher permeability of the edifice and overburden. In contrast, Fig. 3b and c shows higher overpressures due to the decreased permeability of the surroundings.

The strong dependency of gas transport and storage on the rock permeability is highlighted in Fig. 4 depicting gas velocity against permeability in the conduit. The block model is used to plot the variations in gas velocity within the conduit with respect to changes in the wall/dome and conduit permeability. Unsurprisingly, the gas velocity decreases with decreasing permeability, regardless of whether the less permeable regions occur in the conduit or the walls and dome. Fig. 4 shows that for high conduit permeabilities, the gas velocity is controlled by the wall and dome permeabilities, whereas for low conduit permeabilities, the gas velocity is controlled by the low-permeability conduit. However, the conduit permeability is the dominant controller, and the permeability of the surrounding edifice plays a secondary role on the gas velocity.

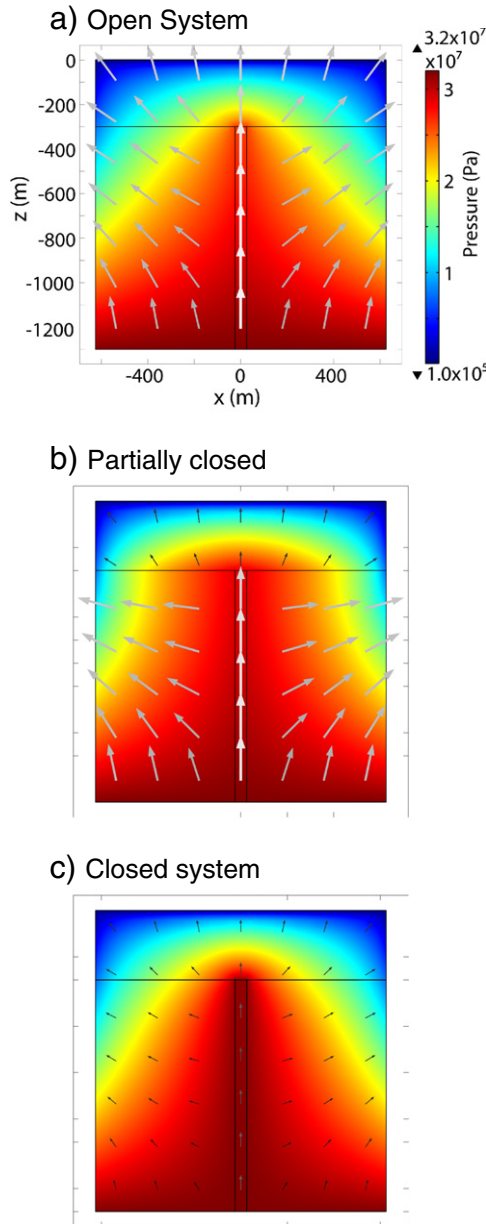


**Fig. 2.** Three block-style models simulating the differences between open and closed degassing systems: a. Open system where the permeabilities in the conduit ( $10^{-10} \text{ m}^2$ ), walls and overburden ( $10^{-12} \text{ m}^2$ ) are sufficient to permit gas transfer. b. The conduit and walls are open with high permeability values of  $10^{-10} \text{ m}^2$  and  $10^{-12} \text{ m}^2$  respectively, whereas the overburden is closed with a very low permeability of  $10^{-16} \text{ m}^2$ . c. Closed system where the permeability of the walls and overburden is very low at  $10^{-16} \text{ m}^2$ . Velocity range of arrows ( $\text{ms}^{-1}$ ): a. max: 0.041, min:  $6.6 \times 10^{-4}$ ; b. max: 0.025, min:  $3.4 \times 10^{-7}$ ; c. max:  $6.4 \times 10^{-6}$ , min:  $4.0 \times 10^{-8}$ .

Figs. 5 and 6 show the principal block model created with an axisymmetric coordinate system. They give a similar result to Fig. 2; however, the pressurisation due to the variation in permeability is lower. In addition, the maximum gas velocity recorded using the axisymmetric system is higher than that using the Cartesian. The open system of Fig. 5 has a maximum velocity of  $0.13 \text{ ms}^{-1}$  compared to  $0.041 \text{ ms}^{-1}$  for the corresponding model in Fig. 2.

Figs. 7 and 8 show vertical pressure profiles for Figs. 2 and 5 respectively. The model using Cartesian coordinates (Fig. 7) shows a greater variation in pressure, and higher pressures are maintained at shallower levels. For the axisymmetric model (Fig. 8), the pressure profiles for the edifice are more linear, showing that they are controlled by the lithostatic pressure. In contrast, the Cartesian models show pressures far

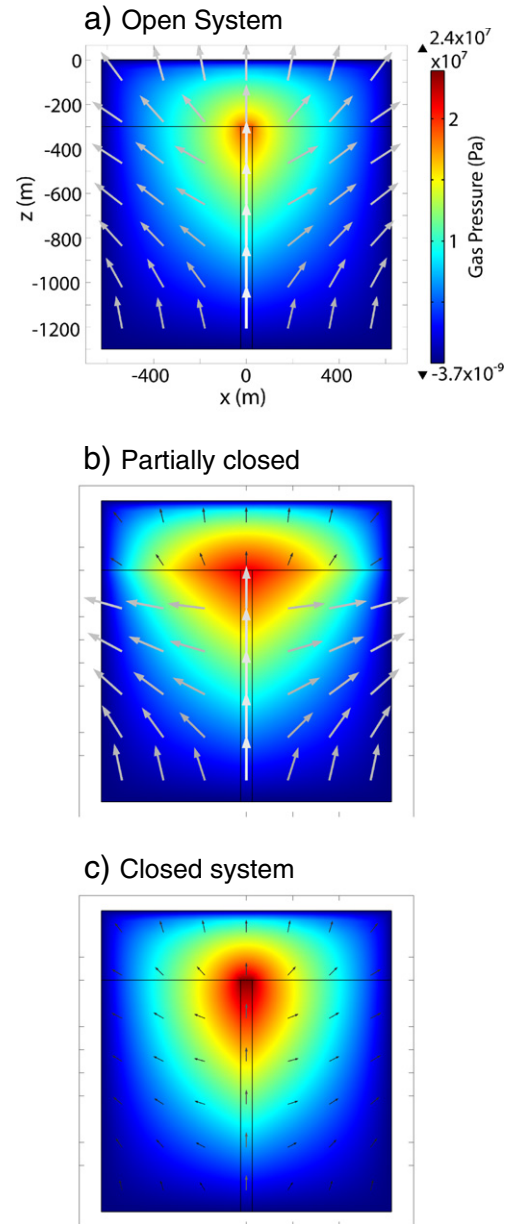


**Fig. 3.** Gas pressure (calculated according to Eq. (6)) for the three models in Fig. 2.

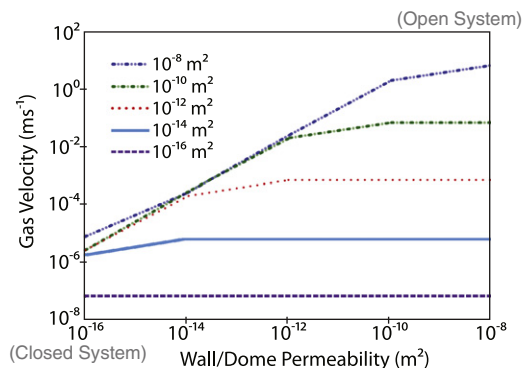


**Fig. 4.** Gas velocity in the centre of the conduit, 600 m below the surface, against wall/dome permeability for different conduit permeabilities.



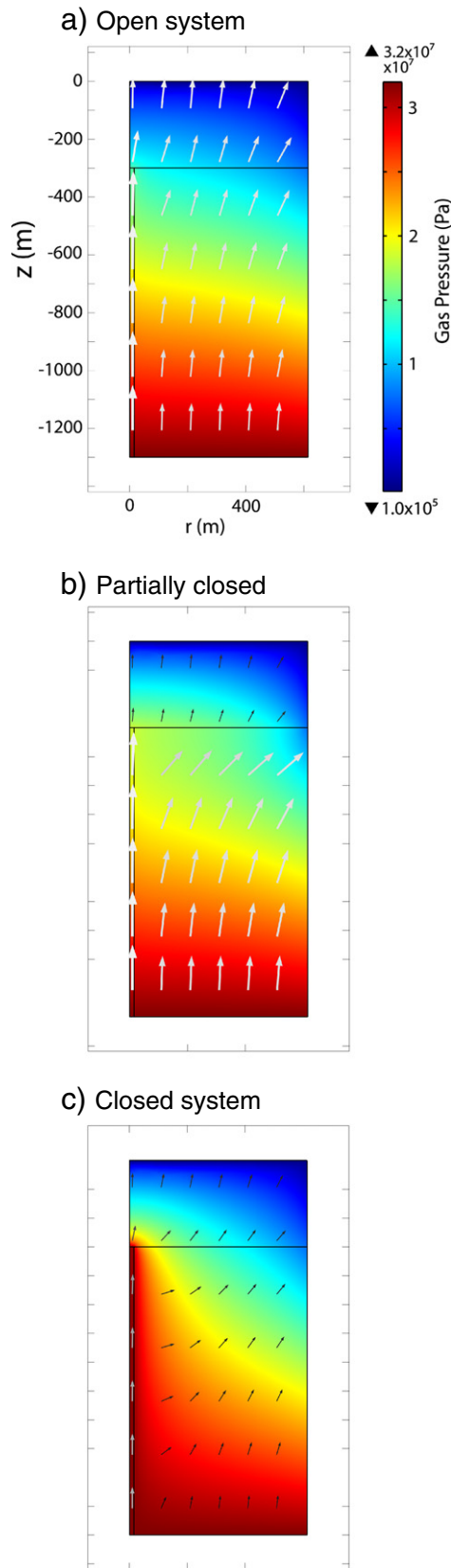


**Fig. 5.** The principal block model solved using an axisymmetric, rather than Cartesian coordinate system. Velocity range of arrows ( $\text{ms}^{-1}$ ): a. max: 0.13, min:  $1.2 \times 10^{-3}$ ; b. max: 0.11, min:  $2.4 \times 10^{-7}$ ; c. max:  $1.5 \times 10^{-4}$ , min:  $7.6 \times 10^{-8}$ .

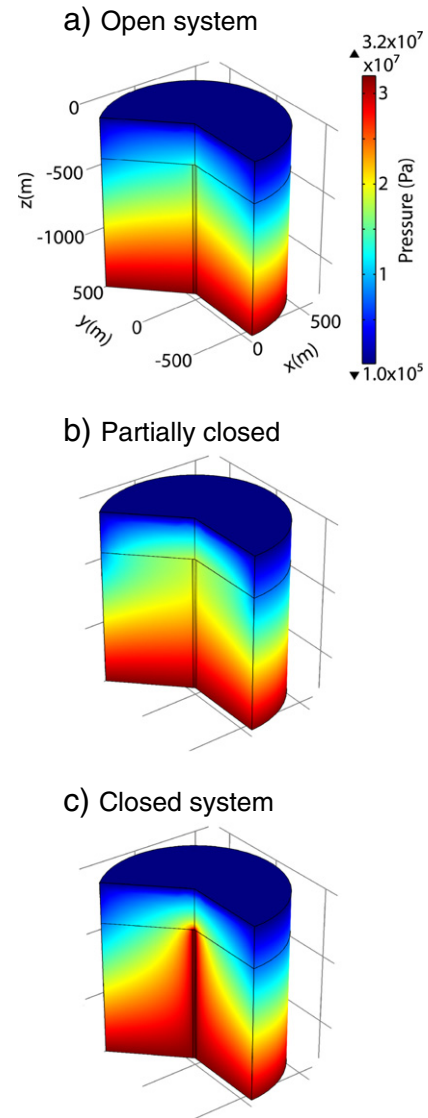


**Fig. 6.** The three-dimensional representations of the axisymmetric models in Fig. 5.

greater than lithostatic, suggesting that the higher pressure from the conduit has a greater influence on the surrounding edifice. In all cases where there is a change in permeability (e.g. conduit to overburden), a sharp change in the pressure gradient is observed.

### 3.2. Sealing gas escape routes

Hydrothermal mineralisation in the dome may lead to sealing of gas escape routes which we model through the introduction of low permeability regions within the dome structure. The system depicted in Fig. 9 represents a dome with a central magma-filled conduit, surrounded by a layered “talus slope” and overlain by a “spine”. Initially all regions of the “talus slope” and the “overburden” have the same permeability, although this is lower than that within the conduit. Rapid sealing of the system is simulated by using a ramp function to decrease the permeability of the “spine” and embedded “talus slope” layers within a time period of 20 min.

Fig. 9a shows a pressure distribution dominated by the permeability-controlled lithostatic pressure. Slight pressurisation of the conduit occurs due to the higher conduit permeability surrounded by less permeable layers. Sealing the specified layers (Fig. 9b) results in a significant alteration to the pressure pattern — all the regions “below” the sealed layers

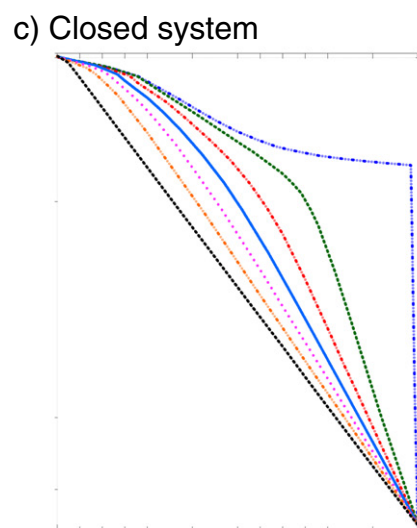
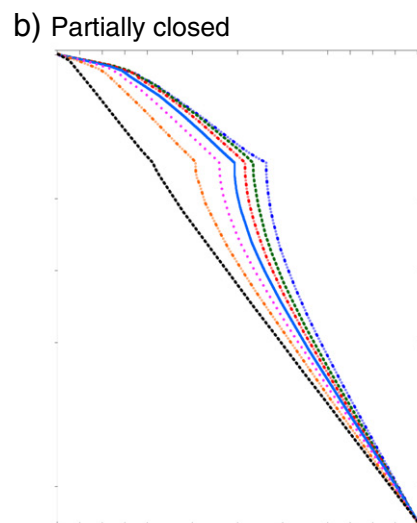
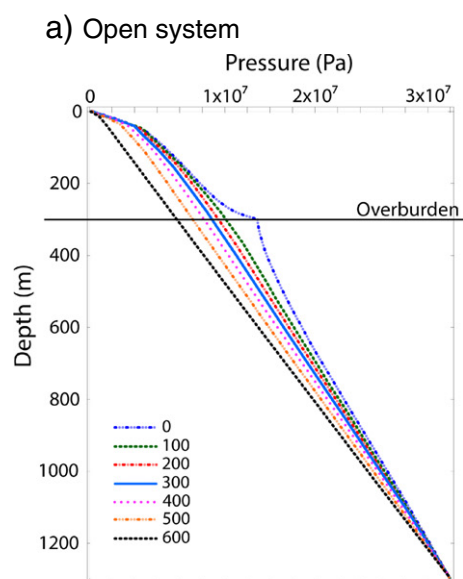
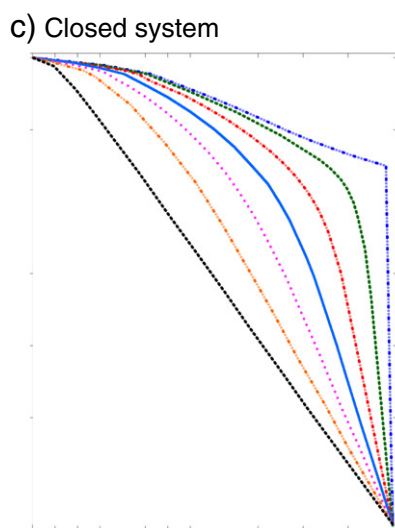
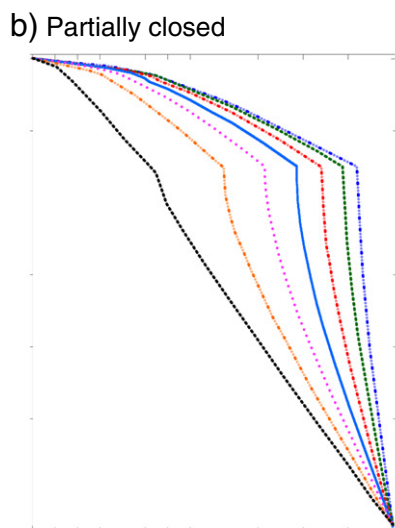
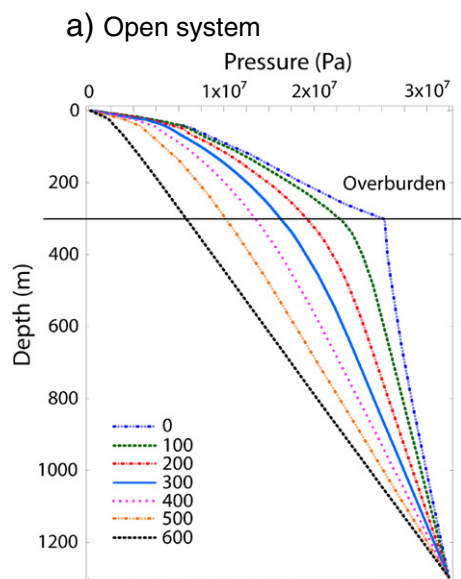
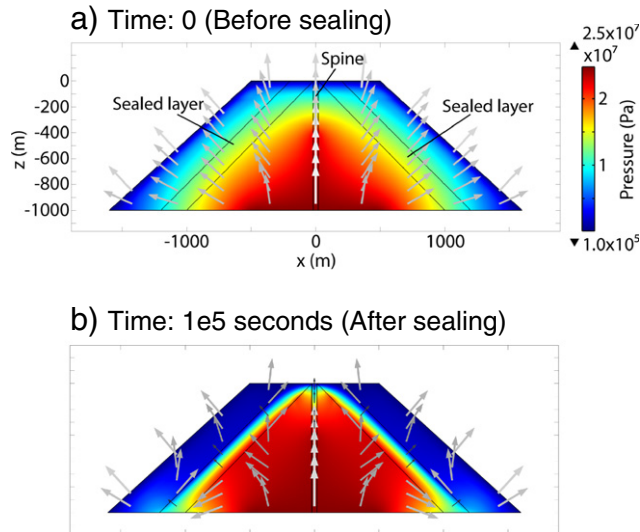


Fig. 7. Vertical pressure profiles for Fig. 2 taken at 100 m intervals between  $x=0$  and  $x=600$  m.

Fig. 8. Vertical pressure profiles for Fig. 5 taken at 100 m intervals between  $r=0$  and  $r=600$  m.



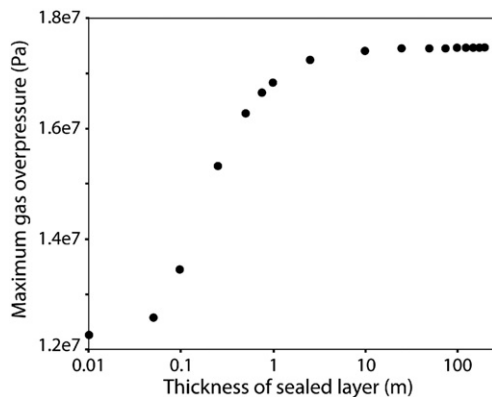
**Fig. 9.** Model to investigate sealing of the system. The images present two snapshots in equilibrium, (a) before and (b) after sealing. The conduit has a permeability of  $10^{-10} \text{ m}^2$ , the higher permeability regions of  $10^{-12} \text{ m}^2$ , and the sealed regions of  $10^{-16} \text{ m}^2$ . Velocity range of arrows ( $\text{ms}^{-1}$ ): a. max: 0.03, min:  $1.0 \times 10^{-4}$ ; b. max:  $8.0 \times 10^{-3}$ , min:  $6.4 \times 10^{-8}$ .

exhibit pressurisation. Gas is channelled around the impermeable “spine”, diverted by the impermeable layers in the “talus slope” and drawn towards the margin between the “spine” and “talus slope”. This model takes approximately 24 h to respond to the change in permeability.

Fig. 10 plots the maximum gas overpressure against the thickness of the sealed layer. For this plot, several models were run where the spine was kept constant, but the thicknesses of the two sealed layers within the edifice were varied between 0.01 and 200 m. The plot shows that the overpressure increases as the thickness of the sealed layers is increased from 0.01 to 10 m. The gas pressure then stabilises at a value of approximately  $1.75 \times 10^7 \text{ Pa}$  and any further increase in the thickness of the sealed layers has limited influence on the gas overpressure.

### 3.3. Cracked dome model

Degassing through a lava dome is investigated through the introduction of “cracks” modelled as narrow zones of high permeability, penetrating into a dome structure (Fig. 11). The permeabilities within the conduit, walls and bulk of the dome are constant, with the conduit being more permeable. Two narrow cracks penetrate into the dome,



**Fig. 10.** Maximum overpressure versus thickness of the sealed layers for the model in Fig. 9. The spine thickness remains constant, whilst the thicknesses of the two sealed layers within the edifice are modified, from 0.01 to 200 m.

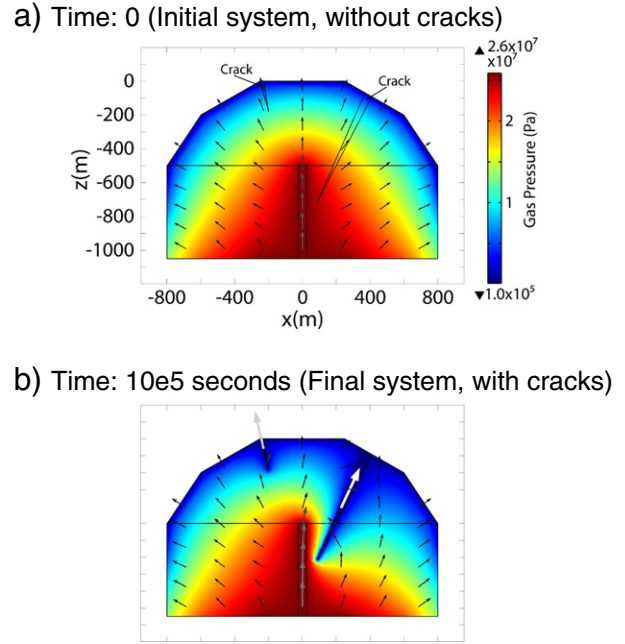


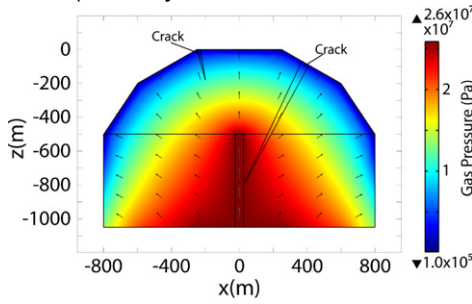
**Fig. 11.** Temporal cracked dome model, comparing the initial crack-free system (a) to the system with cracks (b). The conduit has a permeability of  $10^{-10} \text{ m}^2$ , the walls/dome of  $10^{-14} \text{ m}^2$  and the cracks of  $10^{-8} \text{ m}^2$ . Velocity range of arrows ( $\text{ms}^{-1}$ ): a. max:  $3.3 \times 10^{-4}$ , min:  $1.0 \times 10^{-5}$ ; b. max: 0.15, min:  $1.0 \times 10^{-5}$ .

in which the permeability increases through time from  $10^{-14}$  to  $10^{-8} \text{ m}^2$  via a ramp function. The cracks are modelled as an increase in permeability rather than with atmospheric pressure in order to account for the presence of debris within the cracks. By observing how the system changes through time, the impact of these cracks on the overall pressure and gas flow within the system can be estimated.

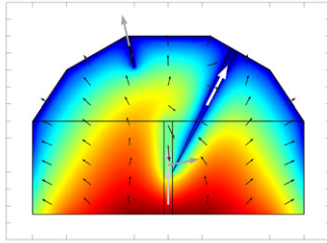
Fig. 11a shows the initial system of a dome without cracks. Consequently the pressure distribution is dominated by the lithostatic pressure coupled with the variations in permeability. The conduit has the higher permeability; therefore, the lower permeability of the surrounding material generates pressurisation (above lithostatic). On crack development (Fig. 11b), there is significant depressurisation around the cracks, and this is proportional to the size and depth of the crack. However, the pressure gradient around the cracks is very high and therefore the pressure decrease within the conduit is very low, only  $1.7 \times 10^4 \text{ Pa}$ . The high permeability of the conduit retains a high pressure, thereby facilitating the continuous storage of gas. Hence the influence of the cracks appears localised, but shows the bulk of the dome may be degassed and depressurised by cracks. Gas flow is significantly higher within the cracks, suggesting that their higher permeability acts to draw the gas from the system. Fig. 12 shows the system where one of the cracks does reach the conduit. In this situation, the conduit is significantly degassed. There is also a dramatic increase in the maximum gas flux recorded in the model. In Fig. 11, the maximum velocity occurs near the exit of the largest crack. In contrast, when the crack reaches the conduit (Fig. 12) the greatest gas flux occurs at the base and exit of the largest crack. The higher conduit permeability is degassed more rapidly than the overlying dome, resulting in a region of higher pressure overlying a region of lower pressure.

Fig. 13 plots the equilibrium time against the edifice permeability. With wall and dome permeabilities of  $10^{-14} \text{ m}^2$ , the system takes 11 days to reach an equilibrium. However, with the conduit permeability unchanged at  $10^{-10} \text{ m}^2$ , increasing the edifice permeability by two orders of magnitude to  $10^{-12} \text{ m}^2$ , this time decreases to a mere 3.8 h.

## a) Time: 0 (Initial system, without cracks)



## b) Time: 6.6e4 seconds (system re-adjusting to cracks)



## c) Time: 10e5 seconds (Final system, with cracks)

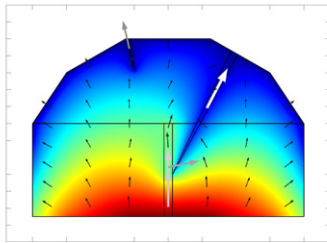


**Fig. 12.** Temporal cracked dome model where the largest crack reaches the conduit: a. the initial crack-free system, b. after 8 h, c. the final system after 11.6 days once the system has attained equilibrium. Velocity range of arrows ( $\text{ms}^{-1}$ ): a. max:  $3.3 \times 10^{-4}$ , min:  $1.0 \times 10^{-5}$ ; b. max: 4.1, min:  $6.8 \times 10^{-6}$ ; c. max: 4.1, min:  $1.1 \times 10^{-5}$ .

### 3.4. Gas escape in fracture zones

Several studies link gas escape to fracture zones that are generated by brittle failure of the magma. Tuffen et al. (2003) propose a mechanism whereby stress accumulation in a viscoelastic magma leads to the generation of fractures in which gas can escape. Gonnermann and Manga (2003) show that magma fragmentation does not always culminate in an explosive eruption. Neuberg et al. (2006) relate the

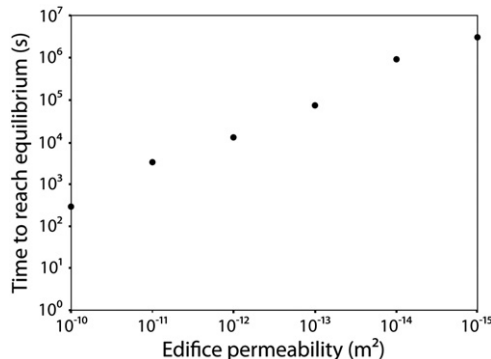


**Fig. 13.** The time for the model to reach equilibrium dependent upon the edifice permeability. Approximate equilibrium times plotted:  $10^{-10}$ : 5 min;  $10^{-11}$ : 1 h;  $10^{-12}$ : 3.8 h;  $10^{-13}$ : 21.8 h;  $10^{-14}$ : 11 days;  $10^{-15}$ : 40 days.

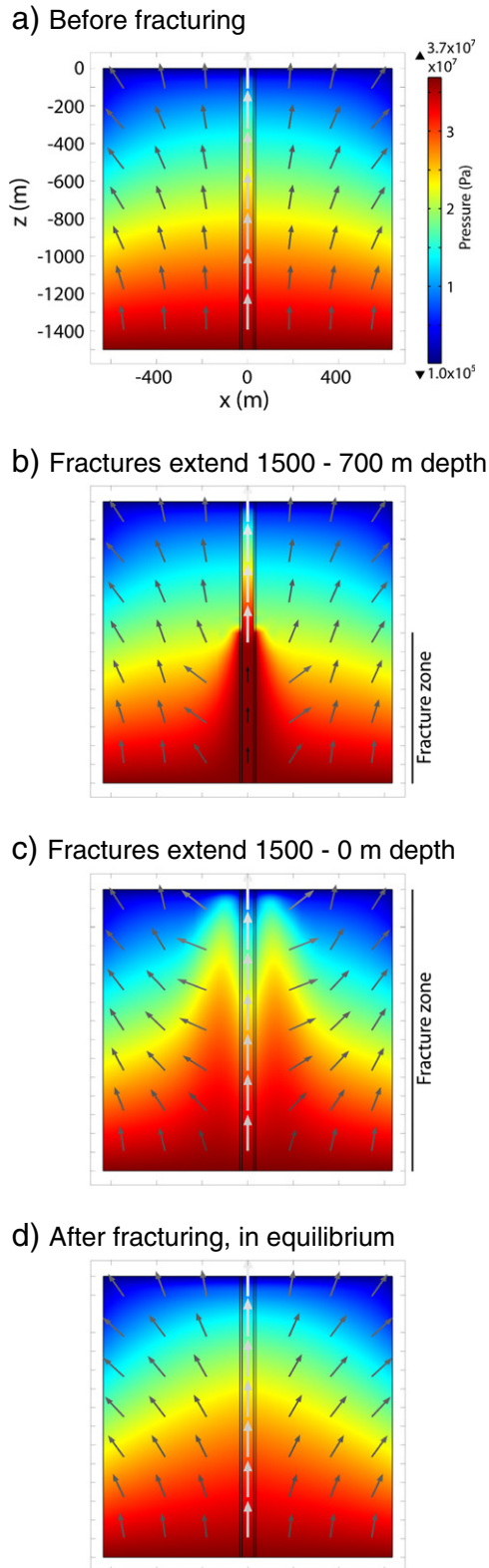
generation of low frequency earthquakes at Soufrière Hills volcano to brittle failure along the conduit-wall boundary. According to these models, brittle failure in magma will produce a system of cracks in a fracture zone along the conduit wall which will act as gas escape routes, resulting in an increase in the permeability within these regions. Lavallée et al. (2008, 2012) show that although the formation of fracture zones does not necessarily lead to acceleration in ascent rate, the acceleration of ascent (and strain) rate does result in the formation of fracture zones. Here, we model the gas response to brittle failure (Fig. 14). Again, a simplistic “block-style” model is used with a central conduit, adjacent to wall rocks. Additionally two 10 m wide domains are added as narrow zones on either side of the conduit. These are regions where an increasing permeability is modelled due to the development of a propagating fracture zone. As magma ascends, a system of shear fractures propagates upwards leading to a domain of increasing permeability. The permeability of the conduit remains higher than that of the walls, and initially, the “fracture zones” have a very low permeability. The fracturing begins at a depth of 1500 m and propagates vertically to the surface over a period of 100 min. The fractures are simulated as an increase in permeability from  $10^{-16}$  to  $10^{-6} \text{ m}^2$ .

Fig. 14a shows the initial system where the pressure distribution and gas behaviour are determined by the lithostatic pressure and variation in permeability. In Fig. 14b the fracture zone has extended upwards to 700 m depth. In response to this brittle failure, the pressure has increased through the conduit and corresponding wall margin where the fractures have developed. This pressurisation is the result of these highly permeable fractures being capped by the unfractured material above. This is another example of regions of high permeability confined by low permeability zones, and provides a suitable environment for the storage of considerable volumes of gas. The pressure also affects the wall margins, but to a lesser degree due to the lower permeability and this fracture development also prompts horizontal gas flow along the wall margin. The fracturing has resulted in a marked change in the gas velocity pattern within the conduit. The high pressure region of the conduit shows only a very low gas flux because of the low pressure gradient. In contrast, the higher pressure gradient at shallower depths within the conduit (before fracturing) forces a much higher gas velocity towards the surface. When the fractures reach the surface (Fig. 14c), the pressure throughout the conduit rapidly decreases. This is accompanied by a rapid expulsion of the stored gas. In contrast, the walls are much slower to respond due to the lower permeability. Fig. 14d shows the system once equilibrium has been resumed, approximately 4 h after the fracture zone reached the surface. Whereas the propagating fracture zone is an effective mechanism for degassing the conduit and wall margins, on attaining equilibrium, the system maintains higher pressure at shallower depth, increasing the capacity for gas storage.

If the propagation of fractures is halted part-way up the conduit, pressurisation continues and accumulates around the fracture margin. Following the model of Neuberg et al. (2006), this does not necessarily increase the potential for further failure, because in their model the formation of shear fractures is triggered by the ascending magma rather than the gas pressure (Holland et al., 2011). However, if the gas pressure reaches a critical pressure, fragmentation could occur. Whilst the pressure conditions within the conduit respond immediately to this pause, the edifice takes a further 1.5 h to react due to the lower permeability.

Fig. 15 shows a similar model to that in Fig. 14. However, the fractures propagate upwards between 1200 m depth and the surface, and are gradually resealed. The initial system is shown in Fig. 15a. In Fig. 15b, the fractures extend between 1200 and 700 m depths. Related to this fracturing, there is an increase in the pressure within the conduit and adjacent walls. However, this pressurisation is not as significant as that seen in Fig. 14b. In Fig. 15c the fracture zone is located between 1200 and 200 m depths. The pressure gradient is very low within the conduit and consequently, there is depressurisation





**Fig. 14.** Brittle failure model, where a system of fractures propagates up the margin from 1500 m depth to the surface. The conduit has a permeability of  $10^{-10} \text{ m}^2$ , the walls of  $10^{-12} \text{ m}^2$ . The fractures are simulated by increasing the permeability of two narrow zones at the conduit margin from  $10^{-16}$  to  $10^{-6} \text{ m}^2$ . Four images are shown from the temporal model: a. the initial system in equilibrium, before fracturing has occurred; b. where the system of fractures has propagated upwards 800 m to a depth of 700 m; c. the fracture zone has reached the surface; d. the system has resumed equilibrium. Velocity range of arrows ( $\text{ms}^{-1}$ ): a. max: 0.30, min:  $1.3 \times 10^{-3}$ ; b. max: 0.38, min:  $8.8 \times 10^{-5}$ ; c. max: 0.33, min:  $6.8 \times 10^{-4}$ ; d. max: 0.30, min:  $9.5 \times 10^{-4}$ .

deeper in the conduit, but pressurisation at shallower levels, associated with the fracturing. When the fractures reach the surface (Fig. 15d), there is instantaneous depressurisation down the conduit and fracture zones. The fractures only extend between 600 m depth to the surface because the fractures have begun to reseat at depth. Fig. 15e has the fractures extending between 200 m and the surface. Whereas in Fig. 15f the fractures have been completely resealed, and the original equilibrium has resumed. This model shows that once fracturing is initiated, the pressure in the conduit and fracture zones increases, due to the overlying sealed regions. However, once the fractures begin to reseat at depth, depressurisation occurs at depth, such that the pressure gradient within the conduit and associated wall margins is very low. It may also be deduced that the degree of pressurisation associated with the fracture zone is dependent upon the length of the fracture zone (Fig. 16), the greater the length of the fracture the greater the gas overpressure.

In Fig. 17, the system of fractures propagates downwards from the surface to a depth of 1500 m, simulating an event where fracturing is initiated by cooling and contraction, and continues to depth. Fig. 17a shows the condition before the event. Again, the fractures develop over a time period of 100 min, and after 50 min the fractures have propagated downwards to a depth of 800 m (Fig. 17b). In contrast to Fig. 14b, a rapid depressurisation of the conduit coincident with the fracturing is evident. The wall margins also show depressurisation, but respond at a decreased rate due to a lower permeability. The very high permeability of the fractures permits a low pressure to penetrate down the conduit and wall margins providing a mechanism for gas extraction. The high pressure gradient within the conduit results in the highest gas flux below the fracture zone. Fig. 17c shows the system after the fractures have reached 1500 m depth. The conduit has reacted rapidly and resumed its equilibrium pressure. In contrast, the wall margins retain a lower pressure, and take a further 4 h to resume equilibrium (Fig. 17d).

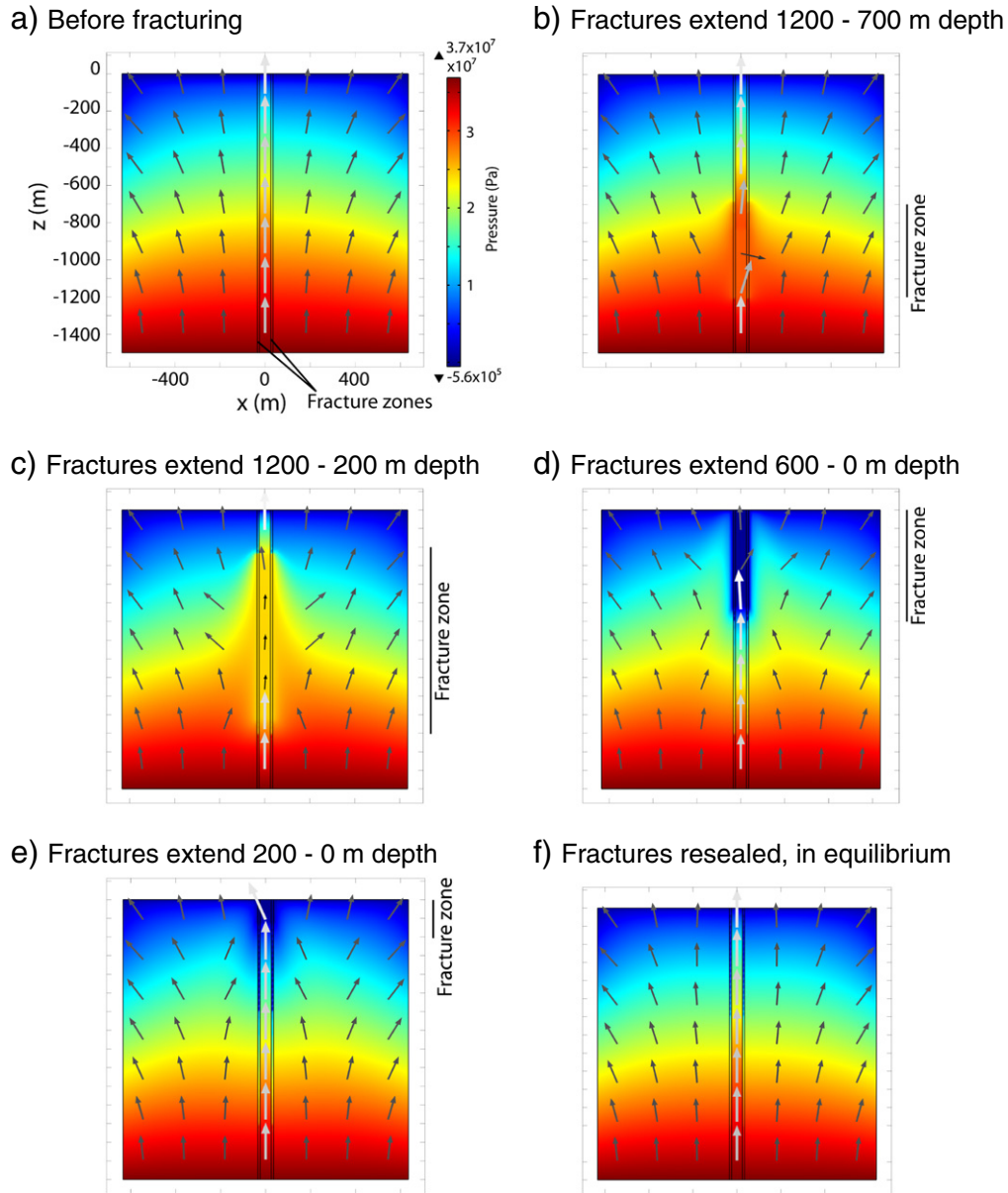
### 3.5. Dome collapse

Dome collapse events are regular occurrences on active silicic volcanoes. They involve either partial or complete removal of the lava dome material and a corresponding unloading and decompression. Whilst a dome collapse comprises a range of complex physical processes, we concentrate on the aspect of unloading and decompression on resident magma.

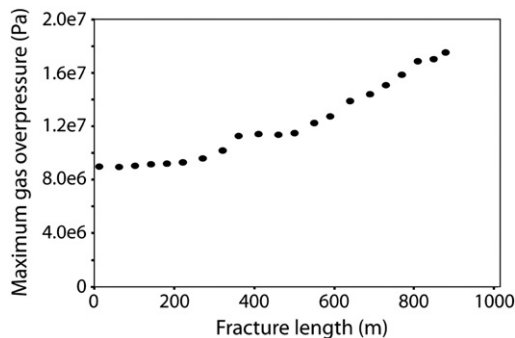
An unloading event is modelled using a “block-style” model (Fig. 18). The permeability in the conduit is higher than the walls, and the overburden is initially sealed by applying a low permeability. The unloading occurs over a period of 20 min with the “removal” of 300 m of dome. This removal is modelled by increasing the permeability of the overburden, from  $10^{-16}$  to  $10^{-6} \text{ m}^2$ . Concurrently, the lithostatic pressure throughout the edifice is decreased to simulate unloading.

Fig. 18a shows the initial state of the model prior to the dome collapse. The impermeable overburden results in pressurisation of the system. Fig. 18b shows the situation once the dome collapse has occurred. The dome collapse event results in decompression of the underlying material, most rapidly within the conduit region of highest permeability. Fig. 18c shows the state of the system after 2 h. The model predicts a significant time lag for the pressure and gas velocity within the edifice to resume equilibrium after the dome collapse (Fig. 18d).

Fig. 19 shows a time history for the period of the dome collapse and afterwards. The plot shows data for three points within the model, located at the base of the dome, centre of the conduit and within the edifice. The plot for the base of the dome is controlled by the decrease in permeability imposed to simulate the collapse. The pressure within the conduit begins to decrease seconds after the onset of the collapse, and continues to decrease steeply. In contrast, it takes several minutes for the pressure within the edifice to respond to the unloading. When it does, the declining pressure within the edifice is more shallow than in the conduit.



**Fig. 15.** Brittle failure model similar to Fig. 14, but fractures begin at 1200 m, propagate upwards and are progressively resealed. The location of the fracture zone is indicated in each plot. The model is represented by 6 snap-shot images: a. the initial system prior to fracturing; b. the system of fractures has developed at 700–1200 m depth; c. 200–1200 m depth; d. 0–600 m depth; e. 0–200 m depth; f. the system once the fractures have been completely resealed, and equilibrium has resumed. Velocity range of arrows ( $\text{ms}^{-1}$ ): a. max: 0.30, min:  $1.2 \times 10^{-3}$ ; b. max: 0.33, min:  $5.5 \times 10^{-4}$ ; c. max: 0.50, min:  $8.8 \times 10^{-5}$ ; d. max: 0.74, min:  $1.1 \times 10^{-3}$ ; e. max: 0.32, min:  $1.3 \times 10^{-3}$ ; f. max: 0.30, min:  $1.3 \times 10^{-3}$ .



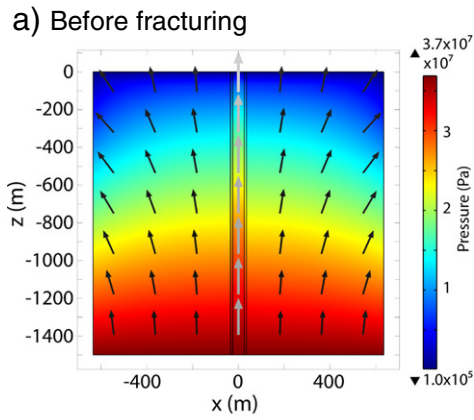
**Fig. 16.** Maximum gas overpressure against the fracture length for Fig. 15. Data taken when fractures are located between 1200 and 310 m below the surface.

The highest gas flux recorded for this model occurred 10 min after the start of the dome collapse, with a peak gas flux of  $90 \text{ ms}^{-1}$ . After this peak, the gas flux drops to 8 to  $15 \text{ ms}^{-1}$ .

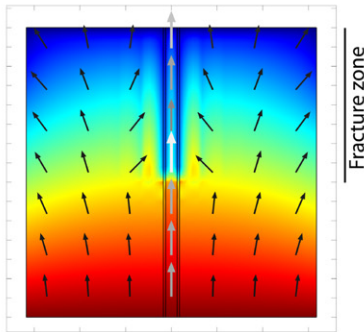
Despite including a source term in this model to account for additional sources of gas due to exsolution, there is no appreciable difference in the behaviour of the model. A decrease in pressure of  $2.45 \times 10^7 \text{ Pa}$ , observed in the conduit of the model during the dome collapse event would correspond to an increase of gas (due to exsolution) of only 1.6 wt.%, or  $40 \text{ kg m}^{-3}$ . A more appreciable difference may be expected if a change in the porosity was included due to the decompressional effects of a dome collapse.

#### 4. Discussion and conclusions

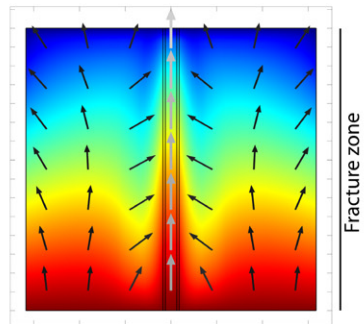
In this study, we adopted a modelling approach to investigate the interaction between the pressure and gas velocity in a medium of



b) Fractures extend 0 - 800 m depth



c) Fractures extend 0 - 1500 m depth



d) After fracturing, in equilibrium

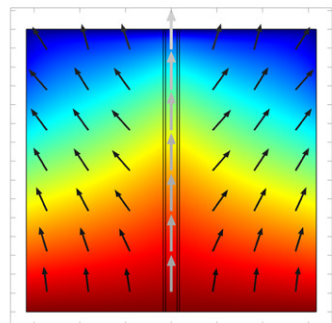
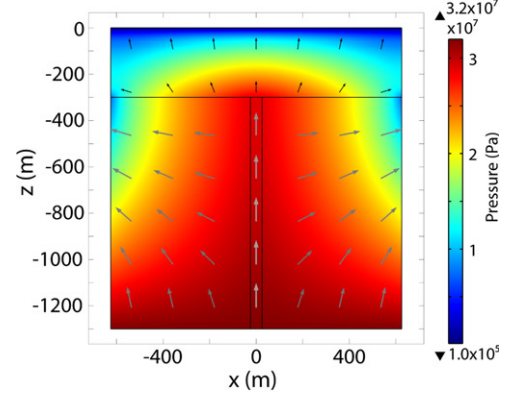
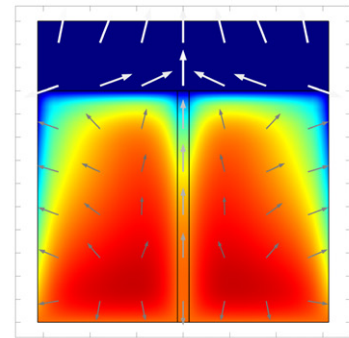


**Fig. 17.** Brittle failure model where the fractures propagate downwards. The conduit has a permeability of  $10^{-10} \text{ m}^2$ , the walls of  $10^{-12} \text{ m}^2$ . The fractures are simulated by increasing the permeability of two narrow zones from  $10^{-16}$  to  $10^{-6} \text{ m}^2$ . The model is represented by 4 snap-shot images: a. the initial system prior to fracturing; b. the system of fractures has propagated downwards to a depth of 800 m; c. fractures have reached a depth of 1500 m; d. equilibrium has been re-established. Velocity range of arrows ( $\text{ms}^{-1}$ ): a. max: 0.30, min:  $1.3 \times 10^{-3}$ ; b. max: 0.78, min:  $1.2 \times 10^{-3}$ ; c. max: 0.30, min:  $1.4 \times 10^{-3}$ ; d. max: 0.30, min:  $1.0 \times 10^{-3}$ .

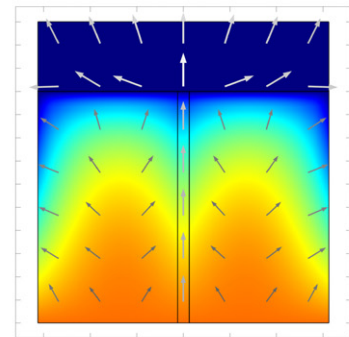
a) Time: 0 (pre-collapse)



b) Time: 20 minutes (post-collapse)



c) Time: 2 hours (post-collapse)



d) Time: 6.5 hours (post-collapse equilibrium)

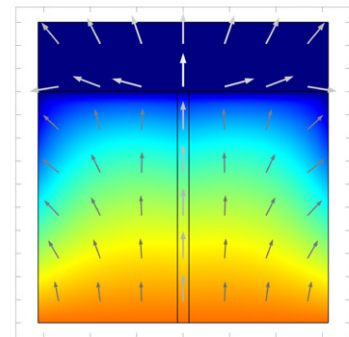


**Fig. 18.** Dome collapse model where the conduit has a permeability of  $10^{-10} \text{ m}^2$ , walls and dome of  $10^{-16} \text{ m}^2$ . The permeability of the dome is increased to  $10^{-6} \text{ m}^2$  to simulate the dome collapse. Velocity range of arrows ( $\text{ms}^{-1}$ ): a. max: 0.025, min:  $3.1 \times 10^{-7}$ ; b. max: 15, min:  $4.8 \times 10^{-4}$ ; c. max: 7.0, min:  $2.9 \times 10^{-4}$ ; d. max: 5.9, min:  $8.3 \times 10^{-4}$ .



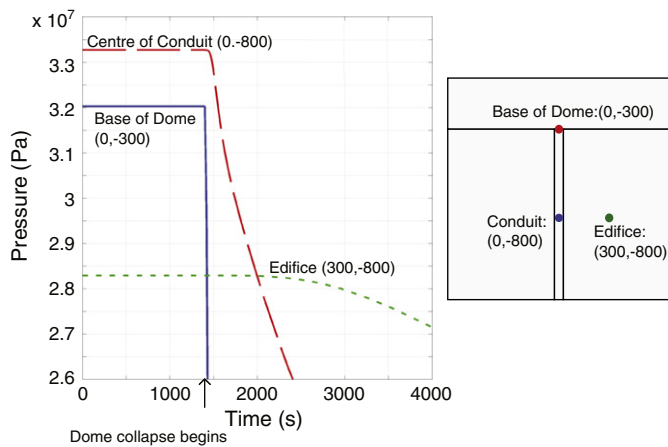


**Fig. 19.** Time sequence for the dome collapse model. Data taken for the centre of the conduit, base of the dome and within the edifice.

variable permeability. Whereas Darcy's law describes the gas velocity as a function of the permeability and pressure gradient, the pressure itself is controlled by the permeability and in turn the permeability of the system is related to the gas content. Hence, the modelling has illustrated that there is a strong interconnection between the structure, permeability and pressure distribution within a volcano, and the resulting gas velocity. Impermeable layers imply not only a barrier to gas transfer, but also a lack of sufficiently high quantities of gas to create degassing pathways. However, if a region of very high permeability is enclosed in such a material, the impermeable layers act to confine the gas, thus increasing its pressure in shallow levels by up to 10 MPa. This process will also increase the magma pressure, increasing the amount of gas dissolved in the melt by up to 1 wt.%. Therefore potentially permitting the storage of high volumes of gas close to the surface, that may be released during a decompressional event such as dome collapse or spontaneous vulcanian explosions (Green and Neuberg, 2005; Linde et al., 2010). Hence, it is obvious that a low permeability layer is necessary to confine volcanic volatiles; however, high pressure and high permeability are also required for effective gas storage. Sealed layers within the walls and dome can result in the gas being deflected and released at the boundaries between regions of different permeability, for example, the margin between fresh dome material and talus slope. Concentrating the gas in this way may lead to weakening associated with hydrothermal alteration. If this occurs at a mechanically critical point within the structure, collapse may occur. Once the gas enters the walls or dome, and a viable exit route exists, loss to the atmosphere may occur from a variety of outlets, for example, cracks in the dome can draw large volumes of gas from the system.

Dome crack development and fracturing down the conduit margin act to draw gas from the system and invoke depressurisation (which could affect dome stability). Whether this occurs passively, or explosively would depend upon the volume of gas stored, where it is located and the confining pressure. This in turn, is strongly determined by the relative permeabilities within the system. The comparison between the two directions in which the fracture zones develop shows a very different behaviour. Ascending magma that triggers shear fracture propagating upward leads to a pressurisation of the magma conduit and gas storage prior to explosive release. In contrast, downwards propagation of the fracture zones promotes depressurisation, gas exsolution and gentle degassing through the edifice.

Even simplistic models used in this study can provide valuable insight into how gas moves through a volcanic system, where it is stored, escapes and where it appears at the surface. Furthermore, these models provide an understanding of the time-dependent response of the magma to sudden pressure changes induced by dome collapse, sealing, and the formation of cracks and fractures. Our models

could be constrained by data sets from ground-based and satellite-platform degassing measurements. Future work will incorporate ground deformation to constrain pressurisation, gas storage and release.

In summary,

- (1) the permeability has a profound impact on the temporal response of the system. The system can take a long time to respond to a crack forming inside the dome. This time is strongly controlled by the edifice permeability. The higher the permeability, the faster the system responds to changes;
- (2) the system can take several hours to resume equilibrium after a dome collapse. However, high gas plumes would be expected simultaneously with the high gas velocities during the collapse, as observed on Soufrière Hills volcano in May 2006 (MVO, 2006). If fragmentation occurs, the system would equilibrate much faster due to the fragmentation wave propagating downwards in the conduit (Fowler et al., 2010);
- (3) a high-permeability region surrounded by low-permeability regions leads to pressurisation which permits greater gas storage at shallow levels;
- (4) in our models, the higher conduit permeability is a dominant controller on the gas flux, whilst the permeability within the surrounding edifice plays a secondary role;
- (5) cracks in the dome structure can be efficient at degassing and depressurising the dome, but their influence is limited. Their influence on the conduit is dependent upon their location and depth. A partial decompression of the dome could affect dome stability;
- (6) upwards propagation of shear fractures leads to pressurisation and storage prior to explosive release, whereas downward propagation promotes depressurisation, gas exsolution and gentle degassing.

## Acknowledgements

This project was funded by NERC PhD studentship (NE/H524673/1). We are grateful to Yan Lavallée and two anonymous reviewers for their constructive comments which greatly improved this paper. Special thanks to Marie Edmonds for her insightful comments which were instrumental for our modelling attempts. We also appreciate the discussions with the Volcano Studies Group within the School of Earth and Environment at the University of Leeds.

## References

- Baxter, P.J., Bonadonna, C., Dupree, R., Hards, V.L., Kohn, S.C., Murphy, M.D., Nichols, A., Nicholson, R.A., Norton, G., Searl, A., Sparks, R.S.J., Vickers, B.P., 1999. Cristobalite in volcanic ash of the Soufrière Hills volcano, Montserrat, British West Indies. *Science* 283, 1142–1145.
- Bernard, M.-L., Zamora, M., Géraud, Y., Boudon, G., 2007. Transport properties of pyroclastic rocks from Montagne Pelée volcano (Martinique, Lesser Antilles). *Journal of Geophysical Research* 112 (B05205).
- Boudon, G., Villemant, B., Komorowski, J.-C., Ildefonse, P., Semet, M.P., 1998. The hydrothermal system at Soufrière Hills volcano, Montserrat (West Indies): characterization and role in the on-going eruption. *Geophysical Research Letters* 25 (19), 3693–3696.
- Bouvet de Maisonneuve, C., Bachmann, O., Burgisser, A., 2009. Characterization of juvenile pyroclasts from the Kos Plateau Tuff (Aegean Arc): insights into the eruptive dynamics of a large rhyolitic eruption. *Bulletin of Volcanology* 71, 643–658.
- Burgisser, A., Gardner, J.E., 2005. Experimental constraints on degassing and permeability in volcanic conduit flow. *Bulletin of Volcanology* 67, 42–56.
- Burgisser, A., Poussineau, S., Arbaret, L., Druitt, T.H., Giachetti, T., Bourdier, J.-L., 2010. Pre-explosive conduit conditions of the 1997 vulcanian explosions at Soufrière Hills volcano, Montserrat: I. pressure and vesicularity distributions. *Journal of Volcanology and Geothermal Research* 194, 27–41.
- Cashman, K., Blundy, J., 2000. Degassing and crystallization of ascending andesite and dacite. *Philosophical Transactions of the Royal Society of London, Series A* 358, 1487–1513.
- Clarke, A.B., Stephens, S., Teasdale, R., Sparks, R.S.J., Diller, K., 2007. Petrological constraints on the decompression history of magma prior to vulcanian explosions at the Soufrière Hills volcano, Montserrat. *Journal of Volcanology and Geothermal Research* 161, 261–274.



- Collombet, M., 2009. Two-dimensional gas loss for silicic magma flows: toward more realistic numerical models. *Geophysical Journal International* 177 (1), 309–318.
- Couch, S., Sparks, R.S.J., Carroll, M.R., 2003. The kinetics of degassing-induced crystallization at Soufrière Hills volcano, Montserrat. *Journal of Petrology* 44 (8), 1477–1502.
- de' Michieli Vitturi, M., Clarke, A.B., Neri, A., Voight, B., 2010. Transient effects of magma ascent dynamics along a geometrically variable dome-feeding conduit. *Earth and Planetary Science Letters* 295, 541–553.
- Edmonds, M., Herd, R.A., 2007. A volcanic degassing event at the explosive-effusive transition. *Geophysical Research Letters* 34 (L21310).
- Edmonds, M., Oppenheimer, C., Pyle, D.M., Herd, R.A., Thompson, G., 2003. SO<sub>2</sub> emissions from Soufrière Hills volcano and their relationship to conduit permeability, hydrothermal interaction and degassing regime. *Journal of Volcanology and Geothermal Research* 124, 23–43.
- Eichelberger, J.C., Carrigan, C.R., Westrich, H.R., Price, R.H., 1986. Non-explosive silicic volcanism. *Nature* 323, 598–602.
- Fischer, T.P., Arehart, G.B., Sturchio, N.C., Williams, S.N., 1996. The relationship between fumarole gas composition and eruptive activity at Galeras volcano, Columbia. *Geology* 24, 531–534.
- Fowler, A.C., Scheu, B., Lee, W.T., McGuinness, M.J., 2010. A theoretical model of the explosive fragmentation of vesicular magma. *Proceedings of the Royal Society of London Series A* 466, 731–752.
- Gonnermann, H.M., Manga, M., 2003. Explosive volcanism may not be an inevitable consequence of magma fragmentation. *Nature* 426, 432–435.
- Gonnermann, H.M., Manga, M., 2005. Nonequilibrium magma degassing: results from modeling of the ca. 1340 A.D. eruption of Mono Craters, California. *Earth and Planetary Science Letters* 238, 1–16.
- Green, D.N., Neuberg, J., 2005. Seismic and infrasonic signals associated with an unusual collapse event at Soufrière Hills volcano, Montserrat. *Geophysical Research Letters* 32 (L07308).
- Heiken, G., Wohletz, K., Eichelberger, J., 1988. Fracture fillings and intrusive pyroclasts, Inyo Domes, California. *Journal of Geophysical Research* 93 (B5), 4335–4350.
- Holland, A.S.P., Watson, I.M., Phillips, J.C., Caricchi, L., Dalton, M.P., 2011. Degassing processes during lava dome growth: insights from Santiaguito lava dome, Guatemala. *Journal of Volcanology and Geothermal Research* 202, 153–166.
- Jaupart, C., 1998. Gas loss from magmas through conduit walls during eruption. In: Gilbert, J.S., Sparks, R.S.J. (Eds.), *The Physics of Explosive Volcanic Eruptions*: Geological Society, London, Special Publications, vol. 145, pp. 73–90.
- Jaupart, C., Allègre, C., 1991. Gas content, eruption rate and instabilities of eruption regime in silicic volcanoes. *Earth and Planetary Science Letters* 120, 413–429.
- Klug, C., Cashman, K.V., 1996. Permeability development in vesiculating magmas: implications for fragmentation. *Bulletin of Volcanology* 58, 87–100.
- Laumonier, M., Arbaret, L., Burgisser, A., Champallier, R., 2011. Porosity redistribution enhanced by strain localization in crystal-rich magmas. *Geology* 39 (8), 715–718.
- Lavallée, Y., Meredith, P.G., Dingwell, D.B., Hess, K.-U., Wassermann, J., Cordonnier, B., Gerik, A., Kruhl, J.H., 2008. Seismogenic lavas and explosive eruption forecasting. *Nature* 453, 507–510.
- Lavallée, Y., Varley, N.R., Alatorre-Ibargüengoitia, M.A., Hess, K.U., Kueppers, U., Mueller, S., Richard, D., Scheu, B., Spieler, O., Dingwell, D.B., 2012. Magmatic architecture of dome-building eruptions at Volcán de Colima, Mexico. *Bulletin of Volcanology* 74, 249–260.
- Linde, A.T., Sacks, S., Hidayat, D., Voight, B., Clarke, A., Elsworth, D., Mattioli, G., Malin, P., Shalev, E., Sparks, S., Widiwijayanti, C., 2010. Vulcanian explosion at Soufrière Hills volcano, Montserrat on March 2004 as revealed by strain data. *Geophysical Research Letters* 37 (L00E07).
- Mader, H.M., Zhang, Y., Phillips, J.C., Sparks, R.S.J., Sturtevant, B., Stolper, E., 1994. Experimental simulations of explosive degassing of magma. *Nature* 372, 85–88.
- Mader, H.M., Brodsky, E.E., Howard, D., Sturtevant, B., 1997. Laboratory simulations of sustained volcanic eruptions. *Nature* 388, 462–464.
- Melnik, O., Sparks, R.S.J., 1999. Nonlinear dynamics of lava dome extrusion. *Nature* 402, 37–41.
- Melnik, O., Sparks, R.S.J., 2002. Dynamics of magma ascent and lava extrusion at Soufrière Hills volcano, Montserrat. In: Druitt, T.H., Kokelaar, B.P. (Eds.), *The Eruption of Soufrière Hills Volcano, Montserrat, from 1995 to 1999*: Geological Society, London, Memoirs, vol. 21, pp. 153–171.
- Melnik, O.E., Blundy, J.D., Rust, A.C., Muir, D.D., 2011. Subvolcanic plumbing systems imaged through crystal size distributions. *Geology* 39, 403–406.
- Mueller, S., Melnik, O., Spieler, O., Scheu, B., Dingwell, D.B., 2005. Permeability and degassing of dome lavas undergoing rapid decompression: an experimental determination. *Bulletin of Volcanology* 67, 526–638.
- Mueller, S., Scheu, B., Spieler, O., Dingwell, D.B., 2008. Permeability control on magma fragmentation. *Geology* 36 (5), 399–402.
- MVO, 2006. Assessment of the hazards and risks associated with the Soufrière Hills volcano, Montserrat. Seventh Report of the Scientific Advisory Committee on Montserrat Volcanic Activity, Part II: Technical Report.
- Neuberg, J.W., Tuffen, H., Collier, L., Green, D., Powell, T., Dingwell, D., 2006. The trigger mechanism of low-frequency earthquakes on Montserrat. *Journal of Volcanology and Geothermal Research* 153, 37–50.
- Papale, P., Moretti, R., Barbato, D., 2006. The compositional dependence of the saturation surface of H<sub>2</sub>O + CO<sub>2</sub> fluids in silicate melts. *Chemical Geology* 229, 78–95.
- Spieler, O., Kennedy, B., Kueppers, U., Dingwell, D.B., Scheu, B., Taddeucci, J., 2004. The fragmentation threshold of pyroclastic rocks. *Earth and Planetary Science Letters* 226, 139–148.
- Stasiuk, M.V., Barclay, J., Carroll, M.R., Jaupart, C., Ratté, J.C., Sparks, R.S.J., Tait, S.R., 1996. Decompression of volatile-saturated rhyolitic magma in the Mule Creek vent, New Mexico, U.S.A. *Bulletin of Volcanology* 58, 117–130.
- Stix, J., Zapata, J.A.G., Calvache, M.V., Cortés, G.P.J., Fischer, T.P., Gómez, D.M., Narvaez, L.M., Ordóñez, M.V., Ortega, A.E., Torres, R.C., Williams, S.N., 1993. A model of degassing at Galeras volcano, Columbia, 1988–1993. *Geology* 21 (11), 963–967.
- Tait, S., Thomas, R., Gardner, J., Jaupart, C., 1998. Constraints on cooling rates and permeabilities of pumice in an explosive eruption jet from colour and magnetic mineralogy. *Journal of Volcanology and Geothermal Research* 86, 79–91.
- Takeuchi, S., Nakashima, S., Tomiya, A., Shinohara, H., 2005. Experimental constraints on the low gas permeability of vesicular magma during decompression. *Geophysical Research Letters* 32 (L10312).
- Taylor, B.E., Eichelberger, J.C., Westrich, H.R., 1983. Hydrogen isotope evidence of rhyolitic magma degassing during shallow intrusion and eruption. *Nature* 306 (5943), 541–545.
- Tuffen, H., Dingwell, D.B., Pinkerton, H., 2003. Repeated fracture and healing of silicic magma generate flow banding and earthquakes? *Geology* 31 (12), 1089–1092.
- Williams-Jones, G., Stix, J., Heiligmann, M., Barquero, J., Fernandez, E., Gonzalez, E.D., 2001. A model of degassing and seismicity at Arenal volcano, Costa Rica. *Journal of Volcanology and Geothermal Research* 108, 121–139.
- Wright, H.M.N., Roberts, J.J., Cashman, K.V., 2006. Permeability of anisotropic tube pumice: model calculations and measurements. *Geophysical Research Letters* 33 (L17316).
- Wright, H.M.N., Cashman, K.V., Gottesfeld, E.H., Roberts, J.J., 2009. Pore structure of volcanic clasts: measurements of permeability and electrical conductivity. *Earth and Planetary Science Letters* 280, 93–104.
- Yoshimura, S., Nakamura, M., 2011. Carbon dioxide transport in crustal magmatic systems. *Earth and Planetary Science Letters* 307, 470–478.